

Whole-device entanglement in a 65-qubit superconducting quantum computer

Gary J. Mooney,^{1,*} Gregory A. L. White,^{1,†} Charles D. Hill,^{1,2,‡} and Lloyd C. L. Hollenberg^{1,§}

¹*School of Physics, University of Melbourne, VIC, Parkville, 3010, Australia.*

²*School of Mathematics and Statistics, University of Melbourne, VIC, Parkville, 3010, Australia.*

(Dated: February 24, 2021)

The ability to generate large-scale entanglement is an important progenitor of quantum information processing capability in noisy intermediate-scale quantum (NISQ) devices. In this paper, we investigate the extent to which entangled quantum states over large numbers of qubits can be prepared on current superconducting quantum devices. We prepared native graph states on the IBM Quantum 65-qubit *ibmq_manhattan* device and the 53-qubit *ibmq_rochester* device and applied quantum readout-error mitigation (QREM). Connected entanglement graphs spanning each of the full devices were detected, indicating whole-device entanglement in both devices. The application of QREM was shown to increase the observed entanglement within all measurements, in particular, the detected number of entangled pairs of qubits found within *ibmq_rochester* increased from 31 to 56 of the total 58 connected pairs. The results of this work indicate full entanglement in two of the largest superconducting devices to date.

INTRODUCTION

In the context of quantum computing, entanglement is usually characterised by the presence of non-classical correlations between qubits [1]. It can be thought of as a resource unique to quantum computation [2–4] that is at the heart of achieving quantum speedup [5–8] as well as playing an important role in fundamental physics – being the phenomenon behind Einstein’s “spooky action at a distance” [9]. The development of noisy intermediate-scale quantum (NISQ) devices [10] is rapidly advancing, with “quantum supremacy” demonstrated on sampling problems [11, 12]. To measure the advance of quantum computer technology, a variety of metrics within the quantum computing literature exist that encapsulate progress in a range of categories such as qubit coherence times, cross-talk, state preparation and measurement, and fidelities of gate operations [13–18]. As the field progresses towards larger multi-qubit systems, an appropriate metric to summarise the performance of a quantum information processor is the generation and characterisation of large entangled states. Such states can be generated in the form of either mixed state bipartite entanglement, where the state is inseparable with respect to all bipartitions of qubits within the system, or the stronger condition of genuine multipartite entanglement (GME), where the state always contains inseparable pure states spanning all of its qubits. These two forms of entanglement are described in more detail in [19]. Alternatively, the detailed structure of entanglement can be determined for a deeper analysis [20]. For systems with full qubit control, large entangled states that have been demonstrated in recent years consist of 16, 18, 20, 27 and 57 qubits in superconducting systems [19, 21–24], 18 qubits in a photonic system [25], 20 and 24 qubits in ion trap systems [26, 27], and 20 qubits in a neutral atom system [28]. Similarly GME has been demonstrated on a variety of devices with the current largest being a 27-qubit GHZ state prepared on the IBM Quantum *ibmq_montreal* device [23].

A variety of superconducting quantum devices [29] are hosted by IBM Quantum’s cloud service [30, 31], ranging in sizes from 1 to 65 qubits. The two largest of these devices are the *ibmq_rochester* and *ibmq_manhattan* devices, consisting of 53 and 65 qubits respectively. Although *ibmq_rochester* has a large number of qubits, the error rates are relatively high in comparison to other IBM Quantum devices, with an average readout error rate of $\sim 14\%$ and coherence times of $T_1, T_2 \sim 53 \mu\text{s}$. The *ibmq_manhattan* on the other hand has relatively low error with an average readout error rate of $\sim 3\%$ and coherence times of $T_1 \sim 57 \mu\text{s}$ and $T_2 \sim 71 \mu\text{s}$. In this work, we investigate the extent to which whole-device entangled quantum states can be prepared on IBM Quantum devices such as *ibmq_rochester* and *ibmq_manhattan*. A native-graph state (which has an edge corresponding to each connected pair of qubits within the device) was prepared on the devices, and quantum state tomography was performed on each pair of connected qubits and their neighbours. Using these measurements, the negativity [32, 33] was calculated to detect entanglement between each pair of connected qubits. The measurement process of reading out physical qubits is imperfect, leading to a significant amount of readout error that can obfuscate the resulting data. This can cause prepared quantum states within the device to appear much less entangled than they actually are. To address this issue, a quantum

* mooneyg@unimelb.edu.au

† white.g@unimelb.edu.au

‡ cdhill@unimelb.edu.au

§ lloydch@unimelb.edu.au

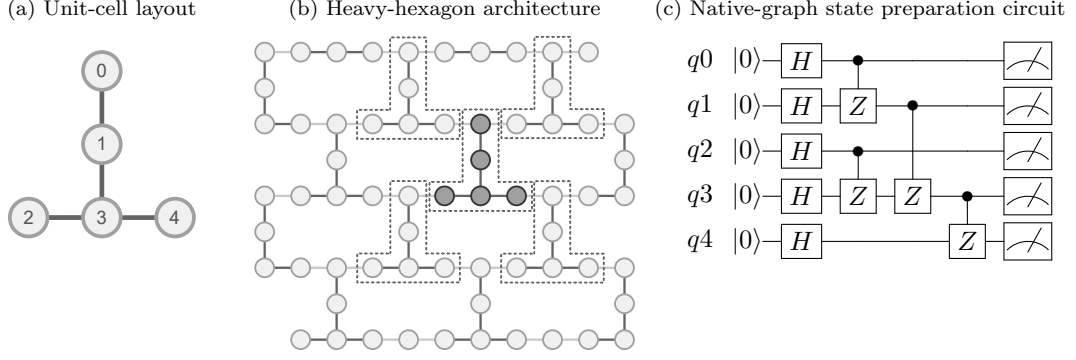


FIG. 1. An example of preparing a native-graph state on a heavy-hexagon unit-cell layout. **(a)** A heavy-hexagon unit-cell layout with q3 being adjacent to q1, q2 and q4. **(b)** The heavy-hexagon architecture for the *ibmq_manhattan* device showing the unit-cell as part of the layout. **(c)** The corresponding circuit to prepare a native-graph state on the heavy-hexagon unit-cell. There are three controlled-phase gates applied to q3, leading to a CNOT depth of three for the circuit. To generate the native-graph state for the full device, the unit-cells can be stitched together by using additional controlled-phase gates without needing to increase the circuit depth.

readout error mitigation (QREM) technique [34] based on quantum detector tomography (QDT) [35] is used to correct raw data. For both devices, we find that the entangled pairs of qubits form connected entangled graphs that include all qubits of the devices, indicating the states were fully entangled. The results for the *ibmq_manhattan* device show clear whole-device entanglement, whether QREM was used or not, with all connected pairs of qubits exhibiting entanglement. However, for the *ibmq_rochester* device, our results indicate that the application of QREM was crucial to mitigate the relatively large readout errors and observe whole-device entanglement, with the number of entangled pairs of qubits increasing from 31 to 56 from the total 58 connected pairs.

RESULTS

Generating and detecting entanglement in graph states

Graph states are entangled states that are defined in relation to a particular connected graph. Vertices represent qubits that are prepared in the $|+\rangle := (|0\rangle + |1\rangle)/\sqrt{2}$ state by applying a Hadamard gate to their initial $|0\rangle$ state and edges represent pairs of qubits that are acted upon by controlled-phase gates. A graph state can be expressed as

$$|G_N\rangle = \prod_{(\alpha,\beta) \in E} CZ_{\beta}^{\alpha} |+\rangle^{\otimes N}, \quad (1)$$

where E is the edge set of the graph G_N corresponding to the N qubit graph state, and CZ_{β}^{α} represents a controlled-phase gate between connected qubits α and β . Graph states have a distinct advantage over other highly entangled states because they can be prepared in parallel, allowing them to be prepared in constant circuit depth with respect to qubit count. Additionally, they have been shown to have entanglement that is more robust against local measurements and noise than Greenberger-Horne-Zeilinger (GHZ) states prepared over the same qubits [36]. To measure the extent of entanglement within a quantum device, we prepare a native-graph state which contains all qubits by having an edge for every connected pair of qubits within the device. An example of how a native-graph state is prepared on a particular system is shown in Figure 1. The CNOT depth of the preparation circuit for a native-graph state is at least as long as the maximum number of neighbouring qubits any single qubit is adjacent to within the device. This is because a controlled-phase gate is applied between the single qubit and each of its neighbours.

To detect bipartite entanglement within the system, instead of using full quantum state tomography on the entire quantum state (which infeasibly scales as 3^N circuits, since there are four basis states for each qubit where measurements that include the I basis can be obtained through post-processing) we show that entanglement is present between partitions of any bipartition of qubits [19, 21]. By measuring the entanglement between every adjacent pair of qubits in the quantum state, an entangled graph can be constructed with edges present only when the pair is found to be entangled. Connected entangled graphs represent entangled clusters of qubits, since they cannot be bipartitioned into disconnected (separable) partitions. The graph representation of the native-graph state for any particular system

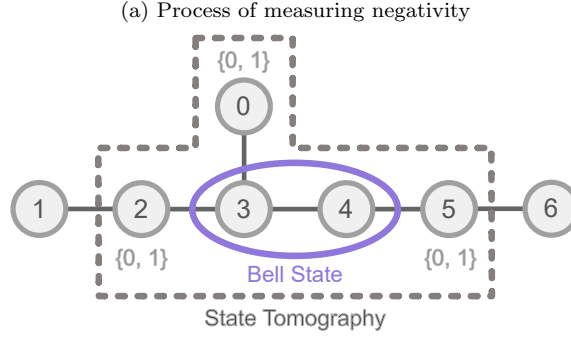


FIG. 2. An example of measuring the negativity between qubits q3 and q4 from an experimentally prepared native-graph state on a particular system. Full quantum state tomography is performed on the pair and their nearest neighbours, that is, qubits q0, q2, q3, q4 and q5. The neighbour qubits q0, q2 and q5 are projected into the Z-basis states 0 and 1 for each possible combination, that is, 000, 001, 010, 011, 100, 101, 110, 111. The negativity is measured for all combinations and the highest negativity is chosen to represent the extent of entanglement between the two qubits. The neighbouring qubits are included in tomography and manually projected in this way because it is important to control which state the qubits are projected into, since different combinations of projected Z-basis states may produce different Bell states. Thus tracing out the neighbouring qubits without projecting them into particular states may cause the remaining 2-qubit state to look maximally mixed.

naturally maximises the number of possible cycles, enabling the corresponding prepared state to tolerate the highest number of non-entangled pairs while still having a connected entangled graph that spans all qubits. Graph states are particularly convenient for measuring the entanglement between adjacent pairs of qubits. They have the property that by projecting all but two qubits of the state, the remaining two qubits can be transformed to a Bell state (up to local transformations) [37]. Entanglement can then be measured between the pair by measuring the negativity [32, 33]. For a quantum state represented as a density matrix ρ , the negativity $\mathcal{N}(\rho)$ between qubit bipartitions A and B can be calculated as

$$\mathcal{N}(\rho) := \sum_i \frac{|\lambda_i| - \lambda_i}{2}, \quad (2)$$

where λ_i are the eigenvalues of the partial transpose of ρ with respect to bipartition B [38]. Two qubits are entangled if and only if the negativity between them is non-zero [39, 40]. To experimentally observe this, quantum state tomography is performed for each adjacent pair of qubits and their neighbouring qubits within the graph state, as shown in Figure 2. Due to imperfections in measurement, the resulting density matrix may have negative eigenvalues, making it non-physical. The nearest physical density matrix under the 2-norm is obtained using an efficient algorithm by Smolin et al. [41]. The neighbouring qubits are then projected onto each combination of Z-basis states to obtain Bell pairs (in principle). These pairs are used to calculate negativities and the largest negativity among the combinations of Z-basis state projections is used to indicate the extent of entanglement within the pair.

Quantum readout error mitigation (QREM)

Due to error introduced during the measurement process, quantum states are often significantly more entangled than indicated by entanglement measures. Even highly entangled states can have measurements fail to detect entanglement. This breakdown can stem from physical errors which may be either classical or quantum in nature, or to a lesser extent, statistical noise due to the limited number of shots. For IBM Quantum devices, it has been shown that the dominant form of measurement noise is classical, motivating a QREM technique used to alleviate measurement error [34]. The measurement noise is represented as a stochastic calibration matrix Λ that contains the conditional probabilities for measuring each erroneous state given each ideally measured state. The calibration matrix is constructed using QDT [35] where combinations of all measurement states are used as the basis states. To build a calibration matrix that considers readout error correlations between all qubits, the number of basis state measurements required is 2^N where N is the number of qubits. For large quantum devices, the number of circuits is too impractical to build the full calibration matrix using QDT. Instead, we assume that the errors are uncorrelated. This allows the calibration matrix, Λ , to be written as

$$\Lambda := \bigotimes_{i=1}^n \Lambda_i \quad (3)$$

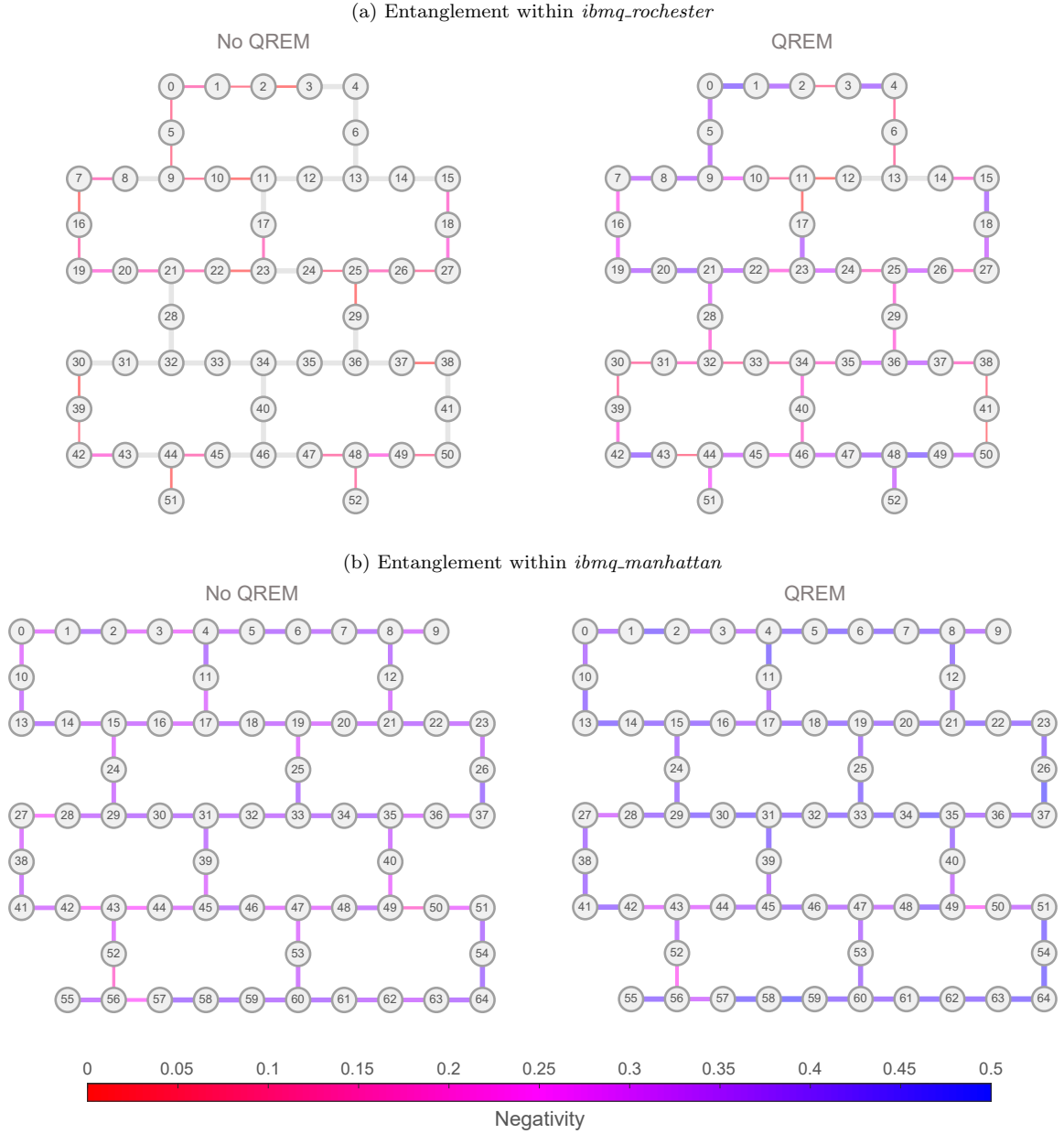


FIG. 3. A graphic visualising the entangled pairs of qubits detected within native-graph states prepared on the 53-qubit *ibmq_rochester* and 65-qubit *ibmq_manhattan* devices. Coloured lines indicate that entanglement was detected between the corresponding pair of qubits with 95% confidence and light grey lines indicate that entanglement was not detected with confidence. Thick blue lines indicate high negativity up to the maximum of 0.5 which corresponds to maximal entanglement, conversely thin red lines indicate low negativity down to a minimum of 0 which corresponds to no entanglement (in which case the edge is coloured light grey). Connected subgraphs induced by entangled pairs as edges are considered to be entangled regions of the device. **(a)** Entanglement within the *ibmq_rochester* device. When quantum readout error mitigation (QREM) was not applied (left), 31 of the 58 pairs were found to be entangled with the largest entangled region consisting of 9 qubits. When QREM was applied (right), a total of 56 out of 58 connected pairs of qubits were found to be entangled with the entangled region consisting of all qubits of the device. The corresponding negativity values used to determine entanglement are shown in Figure 4a. **(b)** Entanglement within the *ibmq_manhattan* device. In both cases of applying and not applying QREM, all 72 pairs of connected qubits were found to be entangled, thus the entangled region includes all qubits of the device. The corresponding negativity values are shown in Figure 4b.

where Λ_i is the calibration matrix for an individual qubit i defined as

$$\Lambda_i := \begin{pmatrix} p(0|0) & p(0|1) \\ p(1|0) & p(1|1) \end{pmatrix}, \quad (4)$$

where the notation $p(x|y)$ indicates the probability of measuring the state $|x\rangle$ given the prepared state $|y\rangle$. This simplification reduces the circuit count to a constant of two since the basis states for each of the qubits can be measured in parallel. In our previous work [23], the assumptions made in performing QREM in this way on a similar IBM Quantum device (27-qubit *ibmq_montreal*) were investigated in detail. These include the assumptions that measurement error is significantly larger than preparation error, that measurement error is predominantly classical, and that measurement error is mostly uncorrelated between qubits. It was shown on sets of four qubits that there were only small differences between full calibration matrices and ones that assume uncorrelated measurement error. This is consistent with another work [34] that showed correlations between readout errors of pairs of qubits on the IBM Quantum’s five-qubit *ibmqx4* device are typically small in most but not all cases. Once the calibration matrix Λ has been constructed, it can be inverted and applied to the measured probability vector \mathbf{p}_{exp} to correct for classical noise. However, the resulting vector is not always physical and may contain negative probabilities due to other forms of noise. To overcome this, the closest physical probability vector \mathbf{p}^* to $\Lambda^{-1}\mathbf{p}_{\text{exp}}$ under the Euclidean norm can be found using the equation

$$\mathbf{p}^* = \arg \min_{\{\mathbf{p}' \mid \forall i \, p'_i \geq 0, \sum_{i=1}^n p'_i = 1\}} (||\Lambda^{-1}\mathbf{p}_{\text{exp}} - \mathbf{p}'||_2). \quad (5)$$

This can be solved by using an efficient algorithm that finds the maximum-likelihood probability distribution to a set of real values summing to one [41].

Entanglement of graph states in the *ibmq_rochester* and *ibmq_manhattan* devices

We perform entanglement detection on the *ibmq_rochester* and *ibmq_manhattan* devices, which consist of 53 and 65 qubits respectively in a heavy-hexagon layout where qubits are located on vertices and edges of a hexagonal grid, as shown in Figure 3. The large numbers of qubits in the devices make them ideal targets for demonstrating the existence of large entangled states. The standard QREM procedure is applied to both devices to help reduce the effects of measurement errors obfuscating entanglement detection. This is especially important for the *ibmq_rochester* device which has comparatively high error rates throughout the device. To measure entanglement, we first prepare a native-graph state containing all qubits and an edge for every connected pair of qubits within the device. The CNOT depth of the preparation circuit for a native-graph state is at least as long as the maximum number of qubits any single qubit is connected to (see Figure 1). For native-graph states in the *ibmq_rochester* and *ibmq_manhattan* devices, the CNOT circuit depths are both three.

For the *ibmq_rochester* device, we perform tomography on all pairs of qubits and their neighbours using circuits consisting of 4000 shots. Additionally, there were two calibration circuits of 8192 shots each performed for QREM. Executions of the experiment were completed within the time period between system calibrations, although we found it unreliable to do so due to the sheer number of circuits. Some circuits were executed considerably later than others, which might affect the data due to error rates of the device drifting over time. In particular, for the *ibmq_rochester* experiments, all tomography circuits were executed before any QREM circuits, which likely reduced the effectiveness of QREM. We successfully completed a total of six full executions of the experiments within calibration times. The results for the best of them are shown in Figure 4a. The figure displays the results for the highest negativity calculated over each combination of Z-basis state projections of neighbouring qubits. The negativity ranges between 0 and 0.5 where 0 indicates no entanglement and 0.5 indicates maximal entanglement. When QREM was applied, full 53-qubit entanglement was detected within the system with 56 of the 58 pairs shown to be above zero negativity with 95% confidence, visualised in Figure 3a. The negativity values with QREM applied had a mean of 0.24 with standard deviation 0.12. When QREM was not applied, 31 of the 58 pairs were found to be significantly above zero negativity with the largest entangled region consisting of 9 qubits. The negativity values in this case had a mean of 0.06 with standard deviation 0.07. The other five experiments on *ibmq_rochester* that ran to completion demonstrated entangled regions of 53, 52, 52, 38, and 21 qubits when QREM was applied.

For the *ibmq_manhattan* device, tomography was performed with the same approach as the *ibmq_rochester* device. Although, to help account for drift noise within the device in the error bars when applying QREM, instead of bootstrapping the calibration data from a single source of measured data, we gathered data for 50 calibration experiments across the execution period and applied QREM from each of them to 50 copies of the tomography data which were then each resampled to become the bootstrapped samples. The calibration experiments were performed such that 25

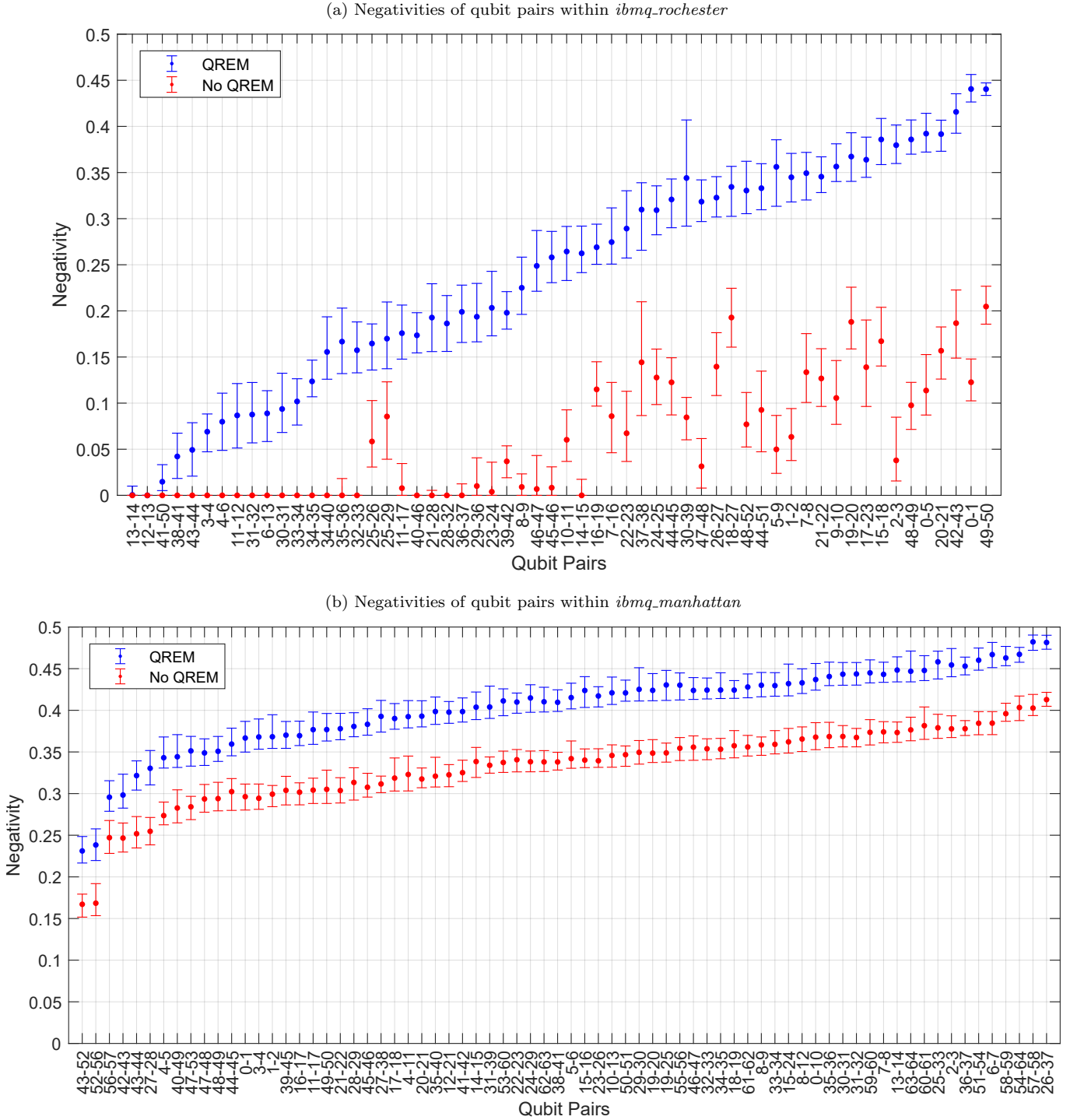


FIG. 4. Negativity experimental results on the IBM Quantum devices showing 53-qubit and 65-qubit entanglement. Each adjacent pair of qubits i and j of the native-graph state is represented as $i-j$ in the figure. The plotted data are the highest negativity values among combinations of neighbouring qubit Z-basis projections between each adjacent pair of qubits. The negativity ranges between 0 and 0.5 where 0 indicates no entanglement and 0.5 indicates maximal entanglement. The 95% confidence intervals are calculated using bootstrapping methods [42, 43]. The data are arranged in ascending order of confidence interval lower bounds in the case of QREM. (a) The negativity results for the *ibmq_rochester* device. Out of the 58 qubit pairs, 56 were found to be entangled when using QREM and 31 when not using QREM. The two qubit pairs 13-14 and 12-13 did not have negativity values significantly above zero in either case of QREM or no QREM. When QREM was applied, the resulting values have mean 0.24 with standard deviation 0.12. When QREM was not applied, the mean is 0.06 with standard deviation 0.07. Detected pairs of entanglement are visualised on the device layout in Figure 3a. (b) The negativity results for the *ibmq_manhattan* device. All 72 of the qubit pairs were found to be entangled in both cases of QREM and no QREM. When QREM was applied, the resulting values have mean 0.40 with standard deviation 0.05. When QREM was not applied, the values have mean 0.33 with standard deviation 0.05. Detected pairs of entanglement are visualised on the device layout in Figure 3b.

were executed before the tomography circuits and 25 were executed afterwards to help account for the difference in readout errors of the device across the execution period. We completed one full execution of the experiment between device calibration times, with results shown in Figure 4b. We found that all 72 of the connected pairs of qubits had negativity above zero with 95% confidence in both cases of applying and not applying QREM. Thus the entangled region of the device clearly included all 65 qubits. The negativity values when QREM was applied had a mean of 0.40 with standard deviation 0.05, and when QREM was not applied, had a mean of 0.33 with standard deviation 0.05. Although the results of this work show full entanglement across the two devices, they are inconclusive as to what level of entanglement is present, for example whether the states are genuinely multipartite entangled.

The confidence intervals for all negativity values in our data are calculated using bootstrapping with bias correction [42, 43]. Without bias correction, we found that the negativity sample estimates were often above the bootstrapped sample means and in some cases were above the bootstrapped confidence intervals entirely. This suggests that the bootstrapped negativity is a biased estimate of the sample negativity when using 4000 shots in the experiments, thus bias correction is used to adjust the confidence intervals to match the negativity estimate. This also suggests that the negativity estimate is biased with respect to the population negativity, thus we could further bias correct the estimate and the confidence intervals upwards again to approximate the population. However, this assumes that the bias between the bootstrap and the sample is the same as the bias between the sample and the population. This extra step is not required to show entanglement within our experiments so we do not use it here. To perform bootstrapping on our data, the data is partitioned into tomography measurement related data and QREM calibration related data. For each bootstrap sample, a copy of the tomography data is made. The QREM data is bootstrapped by resampling with replacement, then applied to each of the copies of tomography data, which are then each resampled once to produce the bootstrapped QREM applied tomography samples. The negativities are then calculated for each sample to produce the final bootstrapped distribution of negativities which are used to calculate the 95% confidence intervals. For pairs of connected qubits with low values of negativity where some of the bootstrapped values are zero, bias correction leaves the bottom of the distribution clamped disallowing bootstrapped values lower than the estimate subtracted by the bootstrap sample mean. This could be a problem for example if all bootstrapped values for the lower bound of the confidence interval are zero, and are bias corrected to be equal to the mean, which may be above zero, leading to the full confidence interval being above zero. To help avoid this problem, the zero values are ignored when calculating the mean of the bootstrap sample negativities, which increases the mean and consequently decreasing the amount of bias correction applied to the bootstrapped sample negativities upwards, leading to a more robust error bar. Applying bias correction did not change whether any of the confidence intervals include the zero negativity value or not, hence the conclusion of these results is unaffected.

DISCUSSION

We prepared native graph states on the IBM Quantum *ibmq-rochester* and *ibmq-manhattan* devices and measured the level of two qubit entanglement across the states. Full quantum state tomography was performed on each connected pair of qubits and their neighbours within the graph states. The neighbouring qubits for each of the pairs were projected onto the Z -basis and the negativities were measured from the resulting density matrix. To reduce the effects of individual qubit noise introduced during the measurement process, we performed the experiments with and without QREM. For the *ibmq-rochester* device, 56 out of 58 of the connected pairs of qubits were found to be entangled when QREM was applied, resulting in the region of entangled qubits spanning all 53 qubits of the device, with a mean negativity of 0.24 and a standard deviation of 0.12. When QREM was not used, 31 out of the 58 connected pairs had a negativity significantly above zero with 95% confidence, resulting in the largest region of entangled qubits consisting of 9 qubits. This signifies the power of QREM in devices with relatively high readout error rates such as the *ibmq-rochester*. For the *ibmq-manhattan* device, all 72 connected pairs of qubits were found to be entangled in both cases of QREM and no QREM, with a mean negativity of 0.40 and a standard deviation of 0.05 when QREM was applied. This indicates that the region of entangled qubits in both cases of QREM and no QREM included all qubits of the device. The results of this work demonstrate the capability of whole-device entanglement within two of the largest IBM Quantum superconducting quantum devices to date and indicate the positive direction towards the physical computation of sizeable and complex quantum algorithms.

ACKNOWLEDGEMENTS

This work was supported by the University of Melbourne through the establishment of an IBM Q Network Hub at the University. CDH is supported by a research grant from the Laby Foundation. We would like to thank Howard

Bondell for valuable discussions on aspects of the statistical analysis.

-
- [1] Ryszard Horodecki, Paweł Horodecki, Michał Horodecki, and Karol Horodecki. Quantum entanglement. *Reviews of Modern Physics*, 81(2):865, 2009.
 - [2] William K Wootters. Quantum entanglement as a quantifiable resource. *Philosophical Transactions of the Royal Society of London. Series A: Mathematical, Physical and Engineering Sciences*, 356(1743):1717–1731, 1998.
 - [3] Peter W Shor. Polynomial-time algorithms for prime factorization and discrete logarithms on a quantum computer. *SIAM Review*, 41(2):303–332, 1999.
 - [4] Robert Raussendorf and Hans J Briegel. A one-way quantum computer. *Physical Review Letters*, 86(22):5188, 2001.
 - [5] John Preskill. Quantum computing and the entanglement frontier. *arXiv preprint arXiv:1203.5813*, 2012.
 - [6] Guifré Vidal. Efficient classical simulation of slightly entangled quantum computations. *Physical Review Letters*, 91(14):147902, 2003.
 - [7] Frank Verstraete and J Ignacio Cirac. Renormalization algorithms for quantum-many body systems in two and higher dimensions. *arXiv preprint cond-mat/0407066*, 2004.
 - [8] Frank Verstraete, Valentin Murg, and J Ignacio Cirac. Matrix product states, projected entangled pair states, and variational renormalization group methods for quantum spin systems. *Advances in Physics*, 57(2):143–224, 2008.
 - [9] Albert Einstein, Boris Podolsky, and Nathan Rosen. Can quantum-mechanical description of physical reality be considered complete? *Physical Review*, 47(10):777, 1935.
 - [10] John Preskill. Quantum computing in the NISQ era and beyond. *Quantum*, 2:79, 2018.
 - [11] Frank Arute, Kunal Arya, Ryan Babbush, Dave Bacon, Joseph C Bardin, Rami Barends, Rupak Biswas, Sergio Boixo, Fernando GSL Brandao, David A Buell, et al. Quantum supremacy using a programmable superconducting processor. *Nature*, 574(7779):505–510, 2019.
 - [12] Han-Sen Zhong, Hui Wang, Yu-Hao Deng, Ming-Cheng Chen, Li-Chao Peng, Yi-Han Luo, Jian Qin, Dian Wu, Xing Ding, Yi Hu, et al. Quantum computational advantage using photons. *Science*, 370(6523):1460–1463, 2020.
 - [13] Steven T Flammia and Yi-Kai Liu. Direct fidelity estimation from few Pauli measurements. *Physical Review Letters*, 106(23):230501, 2011.
 - [14] Marcus P da Silva, Olivier Landon-Cardinal, and David Poulin. Practical characterization of quantum devices without tomography. *Physical Review Letters*, 107(21):210404, 2011.
 - [15] Andrew W Cross, Lev S Bishop, Sarah Sheldon, Paul D Nation, and Jay M Gambetta. Validating quantum computers using randomized model circuits. *Physical Review A*, 100(3):032328, 2019.
 - [16] Mohan Sarovar, Timothy Proctor, Kenneth Rudinger, Kevin Young, Erik Nielsen, and Robin Blume-Kohout. Detecting crosstalk errors in quantum information processors. *Quantum*, 4:321, 2020.
 - [17] Robin Blume-Kohout, John King Gamble, Erik Nielsen, Kenneth Rudinger, Jonathan Mizrahi, Kevin Fortier, and Peter Maunz. Demonstration of qubit operations below a rigorous fault tolerance threshold with gate set tomography. *Nature Communications*, 8:1–13, 2017.
 - [18] Timothy J. Proctor, Arnaud Carignan-Dugas, Kenneth Rudinger, Erik Nielsen, Robin Blume-Kohout, and Kevin Young. Direct randomized benchmarking for multiqubit devices. *Physical Review Letters*, 123:030503, Jul 2019.
 - [19] Gary J Mooney, Charles D Hill, and Lloyd CL Hollenberg. Entanglement in a 20-qubit superconducting quantum computer. *Scientific Reports*, 9(1):1–8, 2019.
 - [20] He Lu, Qi Zhao, Zheng-Da Li, Xu-Fei Yin, Xiao Yuan, Jui-Chen Hung, Luo-Kan Chen, Li Li, Nai-Le Liu, Cheng-Zhi Peng, et al. Entanglement structure: entanglement partitioning in multipartite systems and its experimental detection using optimizable witnesses. *Physical Review X*, 8(2):021072, 2018.
 - [21] Yuanhao Wang, Ying Li, Zhang-qi Yin, and Bei Zeng. 16-qubit IBM universal quantum computer can be fully entangled. *npj Quantum Information*, 4(1):1–6, 2018.
 - [22] Ken X Wei, Isaac Lauer, Srikanth Srinivasan, Neereja Sundaresan, Douglas T McClure, David Toyli, David C McKay, Jay M Gambetta, and Sarah Sheldon. Verifying multipartite entangled Greenberger-Horne-Zeilinger states via multiple quantum coherences. *Physical Review A*, 101(3):032343, 2020.
 - [23] Gary J Mooney, Gregory AL White, Charles D Hill, and Lloyd CL Hollenberg. Generation and verification of 27-qubit Greenberger-Horne-Zeilinger states in a superconducting quantum computer. *arXiv preprint arXiv:2101.08946*, 2021.
 - [24] Bo Yang, Rudy Raymond, Hiroshi Imai, Hyungseok Chang, and Hidefumi Hiraishi. Testing scalable Bell inequalities for quantum graph states on IBM quantum devices. *arXiv preprint arXiv:2101.10307*, 2021.
 - [25] Xi-Lin Wang, Yi-Han Luo, He-Liang Huang, Ming-Cheng Chen, Zu-En Su, Chang Liu, Chao Chen, Wei Li, Yu-Qiang Fang, Xiao Jiang, et al. 18-qubit entanglement with six photons’ three degrees of freedom. *Physical Review Letters*, 120(26):260502, 2018.
 - [26] Nicolai Friis, Oliver Marty, Christine Maier, Cornelius Hempel, Milan Holzäpfel, Petar Jurcevic, Martin B Plenio, Marcus Huber, Christian Roos, Rainer Blatt, et al. Observation of entangled states of a fully controlled 20-qubit system. *Physical Review X*, 8(2):021012, 2018.
 - [27] Ivan Pogorelov, Thomas Feldker, Christian D Marciniak, Georg Jacob, Verena Podlesnic, Michael Meth, Vlad Negnevitsky, Martin Stadler, Kirill Lakhmanskii, Rainer Blatt, et al. A compact ion-trap quantum computing demonstrator. *arXiv preprint arXiv:2101.11390*, 2021.

- [28] Ahmed Omran, Harry Levine, Alexander Keesling, Giulia Semeghini, Tout T Wang, Sepehr Ebadi, Hannes Bernien, Alexander S Zibrov, Hannes Pichler, Soonwon Choi, et al. Generation and manipulation of Schrödinger cat states in Rydberg atom arrays. *Science*, 365(6453):570–574, 2019.
- [29] Morten Kjaergaard, Mollie E Schwartz, Jochen Braumüller, Philip Krantz, Joel I-J Wang, Simon Gustavsson, and William D Oliver. Superconducting qubits: Current state of play. *Annual Review of Condensed Matter Physics*, 11:369–395, 2020.
- [30] IBM. IBM makes quantum computing available on IBM cloud to accelerate innovation. <https://www-03.ibm.com/press/us/en/pressrelease/49661.wss>, 2016. Accessed 23 February 2021.
- [31] IBM Quantum experience. <https://quantum-computing.ibm.com>. Accessed 23 February 2021.
- [32] Martin B Plenio and Shashank Virmani. An introduction to entanglement measures. *Quantum Information & Computation*, 7(1):1–51, 2007.
- [33] Matthias Christandl. The structure of bipartite quantum states-insights from group theory and cryptography. *arXiv preprint quant-ph/0604183*, 2006.
- [34] Filip B Maciejewski, Zoltán Zimborás, and Michał Oszmaniec. Mitigation of readout noise in near-term quantum devices by classical post-processing based on detector tomography. *Quantum*, 4:257, 2020.
- [35] JS Lundeen, A Feito, H Coldenstrodt-Ronge, KL Pregnell, Ch Silberhorn, TC Ralph, J Eisert, MB Plenio, and IA Walmsley. Tomography of quantum detectors. *Nature Physics*, 5(1):27–30, 2009.
- [36] Hans J Briegel and Robert Raussendorf. Persistent entanglement in arrays of interacting particles. *Physical Review Letters*, 86(5):910, 2001.
- [37] Robert Raussendorf, Daniel E Browne, and Hans J Briegel. Measurement-based quantum computation on cluster states. *Physical Review A*, 68(2):022312, 2003.
- [38] Guifré Vidal and Reinhard F Werner. Computable measure of entanglement. *Physical Review A*, 65(3):032314, 2002.
- [39] Asher Peres. Separability criterion for density matrices. *Physical Review Letters*, 77(8):1413, 1996.
- [40] Michał Horodecki, Paweł Horodecki, and Ryszard Horodecki. Separability of n-particle mixed states: necessary and sufficient conditions in terms of linear maps. *Physics Letters A*, 283(1-2):1–7, 2001.
- [41] John A Smolin, Jay M Gambetta, and Graeme Smith. Efficient method for computing the maximum-likelihood quantum state from measurements with additive gaussian noise. *Physical Review Letters*, 108(7):070502, 2012.
- [42] Bradley Efron and Robert Tibshirani. Bootstrap methods for standard errors, confidence intervals, and other measures of statistical accuracy. *Statistical Science*, pages 54–75, 1986.
- [43] Bradley Efron. Nonparametric standard errors and confidence intervals. *Canadian Journal of Statistics*, 9(2):139–158, 1981.